

DNA denaturation bubbles: free-energy landscape and nucleation/closure rates

François Sicard,^{1,2, a)} Nicolas Destainville,^{1,2} and Manoel Manghi^{1,2}

¹⁾ *Université de Toulouse, UPS, Laboratoire de Physique Théorique (IRSAMC), F-31062 Toulouse, France, EU*

²⁾ *CNRS; LPT (IRSAMC); F-31062 Toulouse, France, EU*

The issue of the nucleation and slow closure mechanisms of non superhelical stress-induced denaturation bubbles in DNA is tackled using coarse-grained MetaDynamics and Brownian simulations. A minimal mesoscopic model is used where the double helix is made of two interacting bead-spring rotating strands with a prescribed torsional modulus in the duplex state. We demonstrate that timescales for the nucleation (resp. closure) of an approximately 10 base-pair bubble, in agreement with experiments, are associated with the crossing of a free-energy barrier of $22 k_B T$ (resp. $13 k_B T$) at room temperature T . MetaDynamics allows us to reconstruct accurately the free-energy landscape, to show that the free-energy barriers come from the difference in torsional energy between the bubble and duplex states, and thus to highlight the limiting step, a collective twisting, that controls the nucleation/closure mechanism, and to access opening time scales on the millisecond range. Contrary to small breathing bubbles, these more than 4 base-pair bubbles are of biological relevance, for example when a preexisting state of denaturation is required by specific DNA-binding proteins.

PACS numbers: 87.14.gk, 87.15.H-, 05.70.-a

I. INTRODUCTION

Although the DNA structure in double-helix is robust enough to enable the preservation of the genetic code, it is sufficiently loose to allow the formation of denaturation bubbles, *i.e.* the cooperative opening of a sequence of consecutive base-pairs (bps), even at physiological temperature. DNA opening is central in biological mechanisms such as replication, transcription, repair, or protein binding¹⁻⁴. The magnitude of the interactions between two bases is of a few $k_B T_0$ ($T_0 = 300$ K is room temperature)^{5,6}, and the base-pair opening is closely related to DNA elastic properties. Indeed, a denaturation bubble has much smaller bending and torsional moduli than the double helix one⁷⁻¹⁰. Considering the timescale of DNA replication and transcription (replication rates are roughly 1000 bp/s²), the lifetime of large denaturation bubbles is expected to be on the order of $1 \mu\text{s}$ to 1 ms, as shown in *in vitro* experiments¹¹, where large bubble lifetimes of 20 to $100 \mu\text{s}$ have been observed, even for DNA constructs as small as 30 -bps.

Various numerical and theoretical models have been proposed in the literature to account for the thermodynamic and dynamical properties of denaturation bubbles. DNA denaturation is tackled at different levels of coarse-graining and timescales, going from classical all-atom¹²⁻¹⁴ or coarse-grained (CG)¹⁵⁻¹⁹ molecular dynamics simulations, to mesoscopic models focusing either on the inter-strand distance dynamics²⁰⁻²², or on the bubble size dynamics using the Poland-Scheraga model^{23,24}. However, these approaches did not consider explicitly the twist dynamics and/or were not able to reach the $100 \mu\text{s}$ timescale for long enough sequences. Nonetheless, Mielke

et al.²⁵ studied the interplay between denaturation and writhe, but the applicability of this model was limited to non-equilibrium conditions imposed by the dynamic introduction of torsional stress.

In an attempt to understand the bubble dynamics at the microsecond scale in the absence of supercoiling, a simple CG model, introduced in Ref. 10, showed that long closure times are related to the crossing of a free-

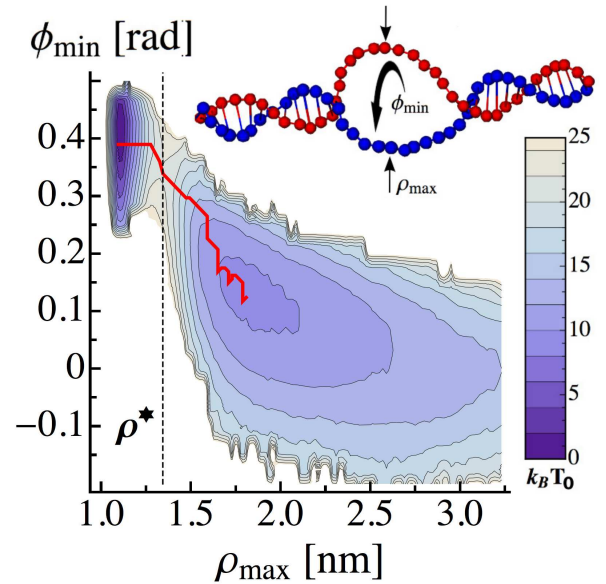


FIG. 1. Free-energy surface associated with the bubble closure/nucleation mechanism projected along two observables ($\beta_0 \kappa_\phi = 580$): the maximal distance between paired bases ρ_{\max} and the minimal twist angle between successive bps, ϕ_{\min} (see inset). The saddle point is located at $\rho^* = 1.35$ nm. The typical minimal free-energy path is shown in red color, and the contour lines are every $2k_B T_0$.

^{a)} Corresponding author: francois.sicard@free.fr.

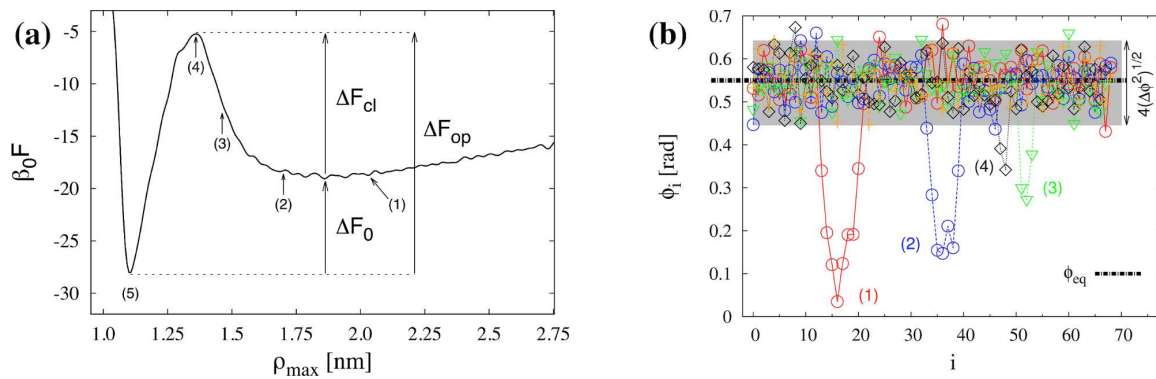


FIG. 2. (a) Free-energy profile associated with the opening/closure mechanism for $\beta_0 \kappa_\phi = 580$. (b) Evolution of the twist angle profile $\phi_i(t)$ for different bubble configurations labelled from (1) to (4) in (a). The fluctuations around the equilibrium value of 0.55 rad [configuration (5)] are represented in grey.

energy barrier from a metastable bubble of ≈ 10 bps to the duplex state. This result accounts for the Arrhenius laws measured experimentally in Ref. 11. Furthermore the role of torsion was highlighted. However, despite the relative simplicity of the model, many processes are still slow to equilibrate due to the presence of a large free-energy barrier, which made the closure a rare event and opening rates inaccessible.

In the present work, Well-Tempered MetaDynamics (WT-metaD)^{26–29}, *i.e.* biased numerical simulations, allow us to study accurately, without these limitations, the thermodynamic and dynamical properties of denaturation bubbles by constructing the whole free-energy landscape, shown in Fig. 1. Whereas most of the theoretical works focused on the dynamics of small breathing bubbles^{20,21,30,31}, we show that the torsion and bending of strands play a pivotal role in the nucleation and closure of bubbles of sizes larger than 4 bps, and which are not superhelical stress-induced^{25,32}. These are of course the denaturation bubbles which are of biological relevance when a long-lived preexisting state of denaturation may be required by specific DNA-binding proteins³³. We highlight that the associated free-energy barrier is of elastic nature, related to single-strand bending and boundary conditions at the bubble extremities, which induce a torsional modulus, $\kappa_\phi^*(L)$, of the whole bubble of length L . This non-vanishing $\kappa_\phi^*(L)$ is shown to be at the origin of the free-energy barriers. For physically relevant model parameters, we find an opening free-energy barrier $\Delta F_{op} = 22 k_B T_0$ and a closure one $\Delta F_{cl} = 13 k_B T_0$. The respective mean opening and closure times are measured numerically^{34,35}: $\tau_{op} = 15 \pm 3$ ms and $\tau_{cl} = 40 \pm 9$ μ s. We emphasize that the so-obtained thermodynamic and dynamical properties are in agreement with experiments¹¹ and biological mechanisms^{36,37}.

II. NUMERICAL MODEL

We use the DNA model of Ref. 10, where the two single strands are modeled as freely rotating chains (FRC)³⁸ of $N = 70$ beads of diameter $a = 0.34$ nm with a AT-rich region of 50 bps clamped by GC regions of 10 bps³⁹. These beads interact through two terms: a Morse potential mimicking the inter-strand hydrogen-bonding and an *effective* intra-strand stacking interaction between the base-pairs modeled through a bare torsional modulus, $\kappa_{\phi,i}(\rho_i)$, that depends on the distance between complementary bases, $\rho_i = |\boldsymbol{\rho}_i| = |\mathbf{r}_i^{(1)} - \mathbf{r}_i^{(2)}|$ with $\mathbf{r}_i^{(j)}$ the position of bead i on strand j , and vanishes for fully separated strands. The evolution is governed by the overdamped Langevin equation. The full Hamiltonian and the details of the numerical implementation and of the parameter values are given in the appendix. Note that, as compared to Ref. 10, model parameters are modified to account for realistic opening times, which were not previously accessible without WT-metaD simulations, but without any direct *a priori* on the closure times. The value of the *bare* torsional modulus, κ_ϕ , in the duplex state, is chosen so that its actual torsional modulus, $\kappa_{\phi,ds}^*$, is close to $450 k_B T_0$, consistent with experimental values⁴⁰. The equilibrium properties of this model are described in Ref. 10 and in the appendix. This model showed that the twist dynamics plays a key role in the closure of pre-equilibrated large bubbles, which occurs in two steps¹⁰: First, the large flexible bubble quickly winds from both ends (*zipping* regime^{10,41}), thus storing bending and torsional energy in the bubble, which stops when it reaches a size of ≈ 10 bps (see Fig. 1). For large κ_ϕ and N , or clamped ends, the ultimate closure of this metastable bubble is then *temperature-activated*¹⁰.

WT-metaD enhances the sampling of the conformational space of a system along a few selected degrees of freedom, named *collective variables* (CVs), and reconstructs the equilibrium probability distribution, and thus the free-energy landscape, as a function of these CVs (see Fig. 1). The chosen CVs must mainly ac-

count for the relevant barriers associated with CG variables on which the free-energy dependence is the most important. Several observables come out naturally to describe the metastable state and the transition to the closed state: (1) the length $L(t)$ of the bubble, *i.e.* the number of opened base-pairs, (2) the width $\rho_{\max}(t)$ of the bubble, *i.e.* the maximal distance between paired bases, (3) the average twist angle per bp in the bubble¹⁰, $\Delta\phi(t) = \langle \phi_i(t) \rangle_{i \in \text{bubble}}$, where the local twist $\phi_i \equiv \arccos\left(\frac{\rho_i \cdot \rho_{i+1}}{\rho_i \rho_{i+1}}\right)$ is the angle between two consecutive base-pair vectors, and (4) the minimal twist angle inside the bubble, $\phi_{\min}(t) = \min_{i \in \text{bubble}} \phi_i(t)$. For numerical efficiency, we choose the width ρ_{\max} as CV to bias the dynamics. Computational details are given in the appendix. To explore the twist dynamics, we choose to follow the evolution of $\phi_{\min}(t)$ instead of $\Delta\phi(t)$, as the latter is very noisy for small bubble sizes and is not defined at all in the closed state.

III. RESULTS

In Fig. 2(a) is shown the free-energy profile associated to the closure mechanism for $\beta_0\kappa_\phi = 580$ ($\beta_0^{-1} = k_B T_0$) along the width $\rho_{\max}(t)$ of the bubble. A *closure* free-energy barrier, ΔF_{cl} , of approximately $14 k_B T_0$ separates the metastable basin associated with the denaturation bubble ($\rho_{\max} \geq 1.35$ nm) from the closed state basin ($\rho_{\max} \approx 1.1$ nm). These two basins are well separated by a standard free-energy of formation $\Delta F_0 \approx 8 k_B T_0$, defining the *opening* free-energy barrier, $\Delta F_{\text{op}} \equiv \Delta F_0 + \Delta F_{\text{cl}} \approx 22 k_B T_0$, associated with the nucleation mechanism. The corresponding evolution of the twist angle profile $\phi_i(t)$ [and thus the minimal twist $\phi_{\min}(t)$] in the bubble is shown in Fig. 2(b). The minimal twist inside the bubble increases when the bubble closes, going from an average value of 0.1 rad (configuration 1) to the ds one, 0.45 rad (configuration 5). In addition to the bubble diffusion along the dsDNA axis, we clearly see that the evolution of $\phi_{\min}(t)$ confirms a *collective twisting* mechanism associated with the existence of the free-energy barrier, *i.e.* $\phi_{\min}(t)$ decreases as $L(t)$ decreases. This mechanism is drastically different from the one at play during the zipping process for which the system is controlled by a *processive twisting*, *i.e.* $L(t)$ decreases while keeping $\phi_{\min}(t) \approx 0$ at the center of the bubble¹⁰. Let us note that switching from AT- to GC-rich region in the model does not change qualitatively the physics of nucleation/closure mechanism, mainly affecting ΔF_{op} .

To go further, we show in Fig. 1 the free-energy surface projected along two observables (ρ_{\max} , ϕ_{\min}), and reconstructed using the *reweighing technique* of Bonomi *et al.*⁴². A typical minimal free-energy path is also shown (in red in Fig. 1) and displays two different regimes. Starting from the metastable basin ($\rho_{\max} \approx 2$ nm), the system is driven by a *collective twisting* (the oblique part of the red path in Fig. 1) up to the saddle point ρ^* . The

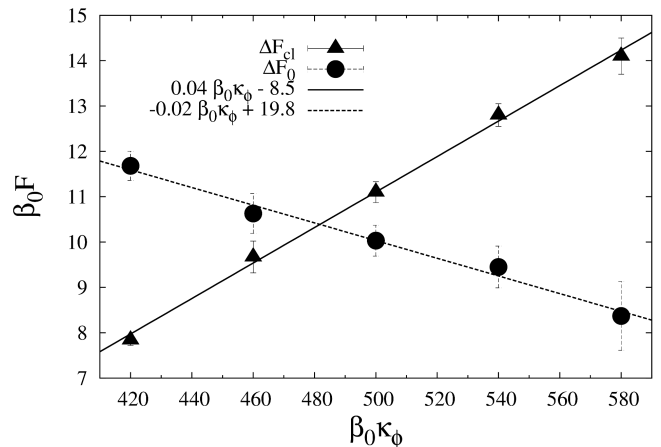


FIG. 3. Evolution of the closure free-energy barrier, ΔF_{cl} (triangles), and the free-energy of formation, ΔF_0 (circles), for increasing values of the *bare* torsional modulus, κ_ϕ . 95% confidence intervals are also provided.

end of the evolution, ($\rho_{\max} < \rho^*$) shows a plateau at $\phi_{\min} = \phi_{\min}^{\text{eq}} \approx 0.4$. This is characteristic of a breathing bubble, *i.e.* the fast opening and closure of a few bps on nanoseconds without modification of the conformation of the whole chain. It precises the previous notion of transient (or breathing) bubble^{20,21,30,31}, and corresponds to bubbles of size $L(t) \leq 4$ bps. To ensure the reliability of the model with experiments, we study in Fig. 3 the dependence of the closure free-energy barrier, ΔF_{cl} , and the free-energy of formation, ΔF_0 , on $\beta_0\kappa_\phi$. As anticipated, the free-energy barriers ΔF_{cl} (resp. ΔF_0), increases (resp. decreases) for increasing values of $\beta_0\kappa_\phi$, scaling affinely in an energy range in agreement with experimental observations¹¹ and biological mechanisms^{36,37}. Therefore, the opening free-energy barrier, ΔF_{op} , increases more slowly than ΔF_{cl} .

Let us now explain the origin of these free-energy barriers. Although the mesoscopic model imposes by hand a vanishing torsional modulus in the ssDNA state, the free-energy barrier is actually related to geometrical constraints: the 2 single strands in the bubble are strongly connected to the double-stranded domain at the edges of the bubble. Indeed, strand stretching and inter-strand interaction lead to an energetic cost associated with the bubble twist. The system can thus be seen as 2 rigid dsDNA arms connected by an effective joint of torsional rigidity $\kappa_\phi^*(L)$ (see Fig. 12 in the appendix). This non-vanishing κ_ϕ^* is responsible for the stop of the zipping process. Actually, the *collective twisting* mechanism associated with the bubble closure is central for the effective joint representation: the double-stranded domains at the edges of the bubble are free to rotate around their own axis to relax the torsional constraint, but not free to rotate relative to one another (as it is the case in the zipping process). This torsional modulus is measured, considering the equipartition theorem, as $\kappa_\phi^* = k_B T / ((\Phi - \langle \Phi \rangle)^2)$, where $\Phi \equiv \sum_{i \in \text{bubble}} \phi_i$ is the twist angle measured *con-*

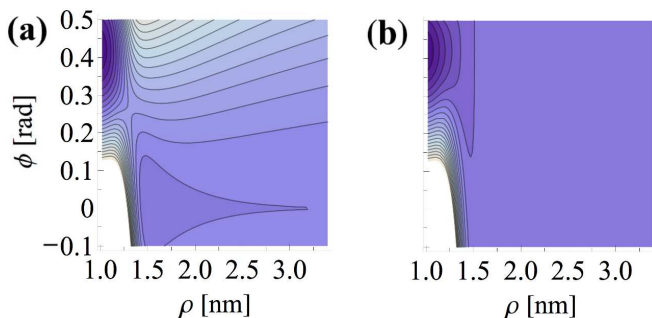


FIG. 4. Energy surfaces of $\mathcal{H}(\rho, \phi)$ associated with the closure mechanism (see text) for $\beta_0\kappa_\phi = 580$, and (a) $\kappa_\phi^* \neq 0$ (to be compared with Fig. 1) and (b) $\kappa_\phi^* = 0$, for which the metastable basin is replaced with a flat free-energy landscape. We use the same free-energy scale as in Fig. 1.

secutively between the bps defining each extremity of the bubble. It is characterized by a non-trivial power law behaviour, $\kappa_\phi^*(L) \propto L^{-\alpha}$ with $\alpha = 2.2 \pm 0.1$, valid down to $L \approx 3$ bps that corresponds to the breathing bubble regime.

The origin of the free-energy barrier is indeed related to the finite value of $\kappa_\phi^*(L)$ in the metastable bubble and the crossover between two minima for the minimal twist angle, ϕ_{\min}^{eq} and 0. Using a mean-field approximation where we consider only the bp located at the center of the bubble, and noting ρ the distance between the two pairing bases and ϕ its twist, we write the following energy:

$$\mathcal{H}(\rho, \phi) = V_{\text{Morse}}(\rho) + \begin{cases} \frac{\kappa_\phi(\rho)}{2}(\phi - \phi_{\min}^{\text{eq}})^2 & \text{for } \rho \leq \rho_b \\ \frac{\kappa_\phi^*(\rho)}{2}\phi^2 & \text{for } \rho > \rho_b \end{cases} \quad (1)$$

with $\rho_b \simeq 1.2$ nm and where V_{Morse} is the Morse potential, and the torsional energy has a bending modulus which depends on the base-pair state: $\beta_0\kappa_\phi \simeq 580$ and $\kappa_\phi^*(\rho) \simeq L(\rho)^{-\alpha}$ (the torsional potential is smoothed with error functions near ρ_b). Note that the dependence of L on ρ is almost linear in the metastable state (see Fig. 11(a) in the appendix). The free-energy surface $\mathcal{H}(\rho, \phi)$ is projected along the two observables (ρ, ϕ) in Fig. 4. We observe a landscape very similar to the one shown in Fig. 1. Moreover, comparing Fig. 4(a) and Fig. 4(b) clearly highlights the role of κ_ϕ^* in the occurrence of the metastable state and the saddle point. Of course this simple model does not account explicitly for the cooperativity between bubble bps and thus yields a crude estimate of free-energy values. Nevertheless, it illuminates the role played by the torsional energy in the closure mechanism in the absence of superhelical stress-induced constraint.

Considering the recent method of Tiwary and Parrinello^{34,35}, we extend the standard application scope of MetaDynamics in order to estimate the rate of transition between the metastable and the closed states (see computational details in the appendix). In Fig. 5 is shown

the evolution of the mean transition times τ_{cl} and τ_{op} (inset) associated with the closure and nucleation mechanisms, as a function of the barrier heights. As expected from the thermodynamic analysis above, τ_{cl} and τ_{op} increase with the height of the free-energy barriers, *i.e.* the value of the torsional modulus $\beta_0\kappa_\phi$. Furthermore, Fig. 5 displays an *Arrhenius-like* exponential dependence of the mean transition times τ_{cl} and τ_{op} on the free-energy of activation, $\tau = \tau_0 \exp(\Delta F/k_B T)$, which follows from Kramers theory⁴³. This exponential dependence remains unchanged with varying values of ρ_b . Actually, in the strong friction regime of interest here, one has $\tau_0 = 2\pi\zeta/(\omega_{\text{met}}\omega_{\text{TS}})$, where ω_{met} (resp. ω_{TS}) is the angular frequency inside the metastable basin (resp. the transition state), and ζ the friction coefficient. The angular frequency ω_{TS} (and consequently τ_0) depends on the choice of the parameters controlling the balance between the hydrogen-bonding and effective stacking interactions (see the appendix). Considering Fig. 9(b) in the appendix, we see that a change of the values of ρ_b does not affect significantly the shape of the transition state and the metastable basin, *i.e.* the angular frequencies ω_{TS} and ω_{met} , only modifying the height of the free-energy barriers. Consequently, this allows us to compare our dynamical analysis with the experimental result of Altan-Bonnet *et al.*¹¹, associated with a characteristic time scale $\tau_{\text{met}}^{\text{exp}} \simeq 50 \mu\text{s}$. One then deduces from Fig. 5 and Fig. 3, $\beta_0\kappa_\phi = 540$, which is significantly different from the value of Ref. 10, because WT-metaD helped us to better set the model parameters, and consistent with hydrogen exchange measurements¹⁸. This value corresponds to an activation free-energy $\Delta F_{\text{op}} \approx 22 k_B T_0$ and a characteristic time scale $\tau_{\text{op}} \approx 15$ ms, for nucleation. Finally, these opening and closure timescales lead to an equilibrium constant $K(T_0) \equiv \tau_{\text{cl}}(T_0)/\tau_{\text{op}}(T_0) \approx 0.003$, comparable with experiments^{11,18,44}. Furthermore, to assert the good matching of the thermodynamic properties

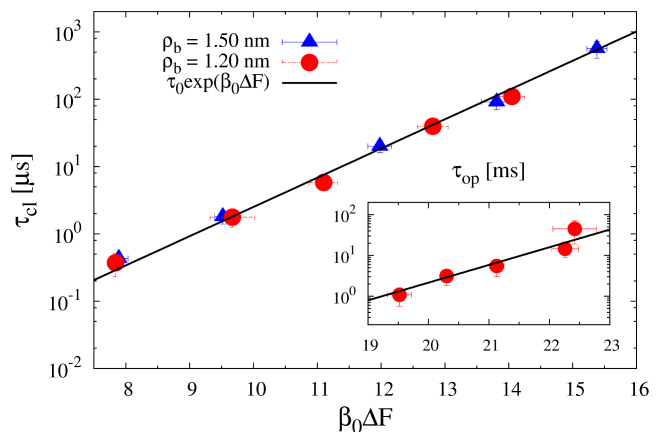


FIG. 5. Mean transition times, τ_{cl} and τ_{op} (closure and nucleation), at room temperature T_0 , as a function of the height of the free-energy barrier ΔF_{cl} , for $\rho_b = 1.20$ nm (circles) and $\rho_b = 1.50$ nm (triangles).

of our model with experiments, we simulated the hairpin of Ref. 44 and found similar melting temperatures (see the appendix). Playing on the model parameters will enable us in a mean future to adjust the thermodynamic and dynamical quantities to different experimental contexts (*e.g.* sequences, ionic strength).

IV. DISCUSSION AND PERSPECTIVES

To go further, it would be interesting to take explicitly into account the role of base stacking in the single-stranded domain. Actually, it is another notable contribution to the energy of stabilization of ssDNA. Therefore, the classical approach considering the ssDNA as a FRC and isotropic hydrogen bonding remains questionable⁴⁵. However, improving our understanding of particular phenomenon with mesoscopic models necessarily reduces the question to fundamental aspects. The use of all-atom simulations, or CG models considering explicitly stacking interaction in the single-stranded domain^{16,19}, coupled to metadynamics, would be interesting, as a second step, to support our mechanism. Furthermore, the role of hydrodynamics interactions⁴⁶, which might accelerate the closure, would be also relevant. Finally, let us comment on the potential biological implications of this work. While strand separation plays a pivotal role in many biological processes, such as replication and transcription, it is commonly accepted that these phenomena are driven primarily by the stresses that are imposed by DNA supercoiling through polymerase actions⁴⁷⁻⁴⁹. However, some biological mechanisms, such as homology recognition³³ or cruciform extrusion⁵⁰, are believed to be dependent of spontaneous DNA-breathing dynamics⁵¹. Therefore, even if negative supercoiling of the dsDNA is assumed to strongly promote the frequency of occurrence and lifetime of DNA-breathing bubbles^{8,52}, there is no definitive evidence that the mechanism highlighted in the present work cannot occur in the absence of supercoiling. It might also be possible that this mechanism takes place to get behind biological mechanisms where DNA would not undergo sufficient torsional stress for bubble nucleation. This roadmap will be considered in the near future.

ACKNOWLEDGMENTS

We acknowledge A.K. Dasanna and P. Rousseau for useful discussions. F.S. thanks J. Cuny and P. Tiwary for fruitful discussions concerning the PLUMED plugin⁵³ and for several very useful suggestions. We acknowledge financial support from the Agence Nationale de la Recherche (Grant No. ANR-11-NANO-010-01).

APPENDIX

Appendix A: Numerical Model

As discussed in Ref. 9, our mesoscopic DNA model consists in two interacting bead-spring chains each made of $N = 70$ beads (of diameter $a = 0.34$ nm) at position \mathbf{r}_i , with a AT-rich region of 50 bps in the middle, and a GC region of 10 bps at each extremity. The Hamiltonian is $\mathcal{H} = \mathcal{H}_{el}^{(1)} + \mathcal{H}_{el}^{(2)} + \mathcal{H}_{tor} + \mathcal{H}_{int}$, where the first two contributions are elastic energies of the strands $j = 1, 2$ which include both stretching and bending energies

$$\mathcal{H}_{el}^{(j)} = \sum_{i=0}^{N-1} \frac{\kappa_s}{2} (r_{i,i+1} - a_{\text{ref}})^2 + \sum_{i=0}^{N-1} \frac{\kappa_\theta}{2} (\theta_i - \theta_{\text{ref}})^2. \quad (\text{A1})$$

The stretching modulus, $a^2 \beta_0 \kappa_s = 100$, is a compromise between numerical efficiency and experimental values⁵⁴, where $\beta_0^{-1} = k_B T_0$ is the thermal energy, $T_0 = 300$ K is the room temperature, and $a_{\text{ref}} = 0.357$ nm. The bending modulus is large, $\beta_0 \kappa_\theta = 600$, to maintain the angle between two consecutive tangent vectors along each strand θ_i to the fixed value $\theta_{\text{ref}} = 0.41$ rad (see Fig. 6). Each strand is thus modeled as a freely rotating chain (FRC). The third and fourth terms of \mathcal{H} are the torsional energy and hydrogen-bonding interactions, respectively. The torsional energy is modeled by a harmonic potential

$$\mathcal{H}_{tor} = \sum_{i=0}^{N-1} \frac{\kappa_{\phi,i}}{2} (\phi_i - \phi_{\text{ref}})^2, \quad (\text{A2})$$

where ϕ_i is defined as the angle between two consecutive base-pair vectors $\boldsymbol{\rho}_i \equiv \mathbf{r}_i^{(1)} - \mathbf{r}_i^{(2)}$ and $\boldsymbol{\rho}_{i+1}$ ($\phi_{\text{ref}} = 0.62$ rad).

The stacking interaction between base pairs is modeled through a $\kappa_{\phi,i}$ that depends on the value of the *bare* dsDNA torsional modulus κ_ϕ , and the distances between complementary bases, $\kappa_{\phi,i} = \kappa_\phi [1 - f(\rho_i) f(\rho_{i+1})]$, where

$$f(\rho_i) = \frac{1}{2} \left[1 + \operatorname{erf} \left(\frac{\rho_i - \rho_b}{\lambda'} \right) \right], \quad (\text{A3})$$

and $\rho_i = |\boldsymbol{\rho}_i|$. Hence, $\kappa_{\phi,i} = \kappa_\phi$ in the dsDNA state and $\kappa_{\phi,i} = 0$ in the ssDNA one. The actual values in the dsDNA state after equilibration, $\kappa_{\phi,ds}^*$, are however different from the prescribed values, κ_ϕ , due to thermal fluctuations and non-linear potentials entering the Hamiltonian. Nevertheless, Fig. 7 underlines the linear correlation between the prescribed and actual values of the torsional modulus, which is representative of the robustness of the mesoscopic model. To compare the mesoscopic model with experiments, we study the dependence on the value of the torsional modulus $\kappa_{\phi,i}$ of the free-energy barrier. In Fig. 8 is shown the evolution of the one-dimensional free-energy profile along the width ρ_{max} for various *bare* torsional modulus, κ_ϕ . As we could expect from a preliminary study¹⁰, the height of the barrier increases as a function of $\beta_0 \kappa_\phi$. This increase of the

height of the free-energy barrier remains local (around the saddle region), and does not affect significantly the shape of the metastable basin.

As shown in Fig. 9, the thermodynamic properties of the model are also sensitive to the values of the parameters λ' and ρ_b defined in Eq. (A3); the latter playing a crucial role on the height of the energy barrier on both sides of the saddle region. Let us note, however, that a change in these values does not change qualitatively the *physics* of the model, *i.e.* the mechanism of nucleation and closure of long denaturation bubble. Considering preliminary simulations, we have chosen $\lambda' = 0.15$ nm and a range of $\rho_b \in [1.20 \text{ nm}, 1.50 \text{ nm}]$. In this work, we mainly focus on $\rho_b = 1.20$ nm, which yields thermodynamic and dynamical properties in good agreement with biophysical mechanisms, *i.e.* to account for realistic opening times, but without any direct *a priori* on the closure times that emerge from Libchaber's experiment¹¹. Playing on the values of ρ_b and κ_ϕ would enable one to adjust the values of ΔF_0 and ΔF_{cl} to different experimental contexts (*e.g.*, sequences, ionic strength). The hydrogen-bonding interaction is modeled by a Morse potential

$$\mathcal{H}_{int} = \sum_{i=0}^{N-1} A \left(e^{-2\frac{\rho_i - \rho_{ref}}{\lambda}} - 2e^{-\frac{\rho_i - \rho_{ref}}{\lambda}} \right), \quad (\text{A4})$$

where $\rho_{ref} = 1$ nm, $\lambda = 0.2$ nm, and $\beta_0 A = 8$ and 12 for AT and GC bonding, respectively, as in Refs. 10 and 41. The fitted values for the dsDNA persistence length and the pitch are $\ell_{ds} \simeq 160$ bps and $p = 12$ bps for the relevant range of $\beta_0 \kappa_\phi$ we are interested in, which are comparable to the actual dsDNA values ($\ell_{ds} \simeq 150$ bps and $p = 10.4$ bps). The ssDNA persistence length is $\ell_{ss} = 3.7$ nm, compatible with experimental measurement⁵⁵, even though in the upper range of measured values.

The evolution of $\mathbf{r}_i(t)$ is governed by the overdamped Langevin equation, integrated using a Euler's scheme,

$$\zeta \frac{d\mathbf{r}_i}{dt} = -\nabla_{\mathbf{r}_i} \mathcal{H}(\mathbf{r}_j) + \xi(t), \quad (\text{A5})$$

where $\zeta = 3\pi\eta a$ is the friction coefficient for each bead of diameter a with $\eta = 10^{-3}$ Pa.s the water viscosity. The diffusion coefficient, $D_{diff} \equiv k_B T_0 / 3\pi\eta a$, thus takes into account the level of coarse-graining of the mesoscopic model involved in the kinetics associated to the smoothed free-energy landscape⁵⁶. The random force of zero mean $\xi_i(t)$ obeys the fluctuation-dissipation relation $\langle \xi_i(t) \cdot \xi_j(t') \rangle = 6k_B T \zeta \delta_{ij} \delta(t - t')$. Lengths and energies are made dimensionless in the units of $a = 0.34$ nm and $k_B T_0$, respectively. The dimensionless time step is $\delta\tau = \delta t k_B T_0 / (a^2 \zeta)$, set to 5×10^{-4} ($\delta t = 0.045$ ps) for sufficient accuracy^{10,41}. This set of parameters induces zipping velocities $v \approx 0.2 - 2$ bp/ns, compatible with experimental measurements⁵⁷.

Appendix B: Melting Temperature

Following Refs. 11 and 44, we focus on the melting dynamics considering the mesoscopic model and DNA beacon configurations (see left panel in Fig. 10). We consider a system made of $N = 35$ beads with a different base sequence from the one considered in the main text to study bubble denaturation: a GC-rich region at the extremity, a AT-base-pair region in the middle, and a T-rich region for the loop. It is indeed analogous to the sequence $5' - GCGCG(AT)_9 GCGC(T)_{12} CGCG(AT)_9 CGCGC - 3'$ considered in Ref. 11, even if the mesoscopic model does not distinguish explicitly the bases A and T (G and C respectively). The length of the loop region has been chosen such that it is greater than the single-stand persistence length $\ell_{ss} \approx 10$ bps.

We study the melting properties associated with end-tagging (GC clamp) and internal-tagging (AT domain), *i.e.* the number of open/closed bps as a function of the temperature. We thus assume that the DNA melting occurs when the average number of bps in the denaturation domain under consideration (AT or GC) is comparable with half of the number of DNA bps in this domain (see right panel in Fig. 10). Considering the parameters $\beta_0 \kappa_\phi = 580$ and $\rho_b = 1.20$ nm, that mainly control the width of the equilibrium well and the height of the energy barrier, one obtains $T_m^{AT} \approx 330$ K and $T_m^{GC} \approx 338$ K. It is well known that the melting temperature is sensitive to the salt concentration in the system. Then, if we consider that the *implicit* salt condition of our system is representative of a screened system, our result is compatible with experimental measurement, $T_m^{\text{internaltag}} \approx 345$ K and $T_m^{\text{endtag}} \approx 350$ K.¹¹

Appendix C: MetaDynamics Simulations

Thermodynamic properties. Because of its convergence properties, Well-Tempered MetaDynamics (WT-metaD) is the most widely adopted version of the metadynamics algorithm²⁸. In WT-metaD, the bias deposition rate decreases over simulation time and the dynamics of all the microscopic variables becomes progressively closer to thermodynamic equilibrium as the simulation proceeds, making the bias to converge to its limiting value in a single run and avoiding the problem of overfilling, *i.e.* when the height of the accumulated Gaussians largely exceeds the true barrier height. Thus one prevents the system from being irreversibly pushed in regions of configuration space which are not physically relevant. Its success depends on the critical choice of a reasonable number of relevant collective variables (CVs). All the relevant slow varying degrees of freedom must be described by the CVs. In addition, the number of CVs must be small enough to avoid exceedingly long computational time, while being able to distinguish among the different conformational states of the system. However, to correctly describe the free-energy landscape, it is not

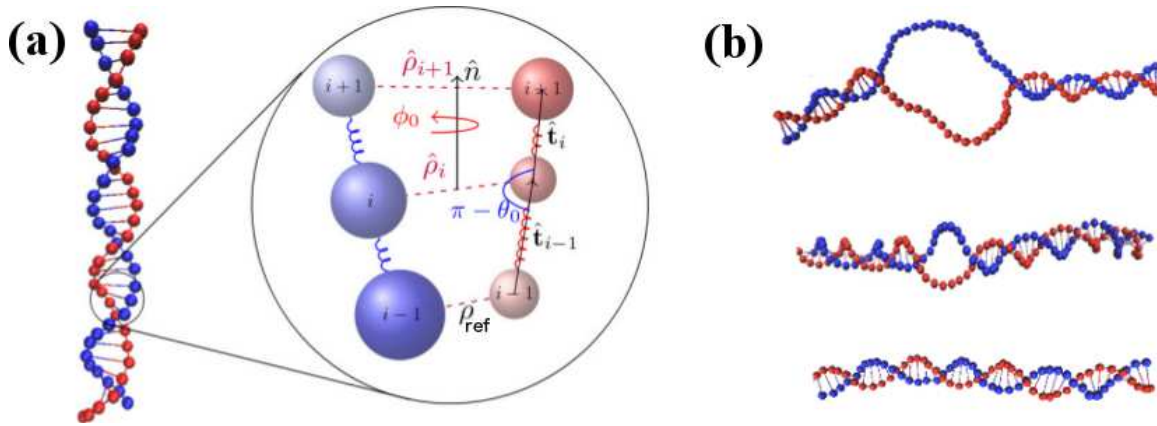


FIG. 6. (a) Snapshot of an equilibrated double helix (from Ref. 10). The bending angle along each strand is θ_{ref} , ρ_{ref} is the equilibrium base-pair distance and \hat{n} is the helical axis around which twist is defined. The imposed equilibrium twist between successive pairs is ϕ_{ref} . (b) Graphic representation of the evolution of the bubble closure/nucleation.

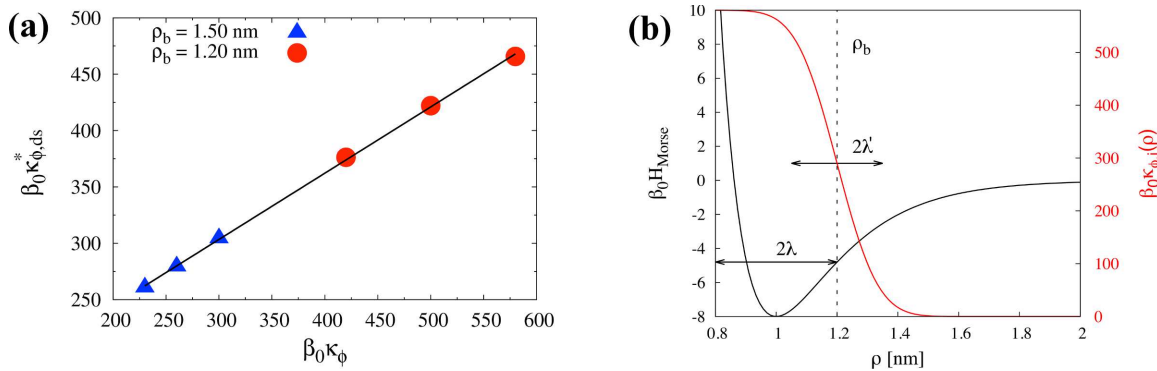


FIG. 7. (a) Evolution of the actual torsional modulus, $\kappa_{\phi,\text{ds}}^*$, of dsDNA, as a function of the *bare* torsional modulus, κ_{ϕ} , for $\rho_b = 1.50$ nm (triangles) and $\rho_b = 1.20$ nm (circles): $\kappa_{\phi,\text{ds}}^* = (0.59 \pm 0.01)\kappa_{\phi} + (127 \pm 3)$. As expected from the definition of the stacking interaction in Eq. (A3), the value of ρ_b does not play a role in the duplex state. (b) Representation of the hydrogen-bonding interaction modeled by a Morse potential (black curve) and the stacking interaction between base pairs (red curve). The choice of the internal parameters ($\lambda, \rho_{\text{ref}}$) and (λ', ρ_b) fixes the transition between stacked and unstacked regime taking into account local denaturation.

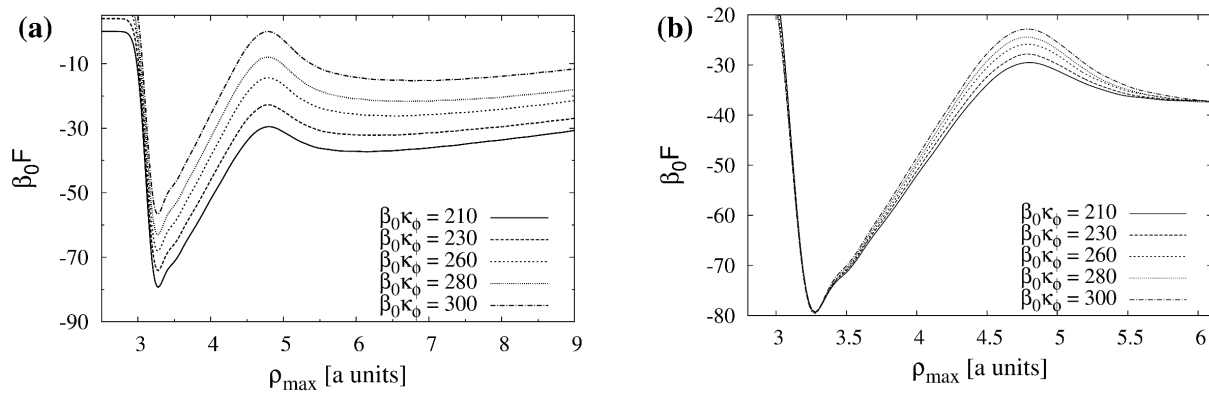


FIG. 8. Evolution of the free-energy profile associated with the temperature-activated closure mechanism for increasing values of $\beta_0 \kappa_{\phi}$, and $\rho_b = 1.50$ nm. (a) The free-energy profiles are shifted arbitrarily along the ordinate axis for clarity. (b) The free-energy profiles are fitted with respect to the closed-state basin to underline the increase of the barrier height with $\beta_0 \kappa_{\phi}$.

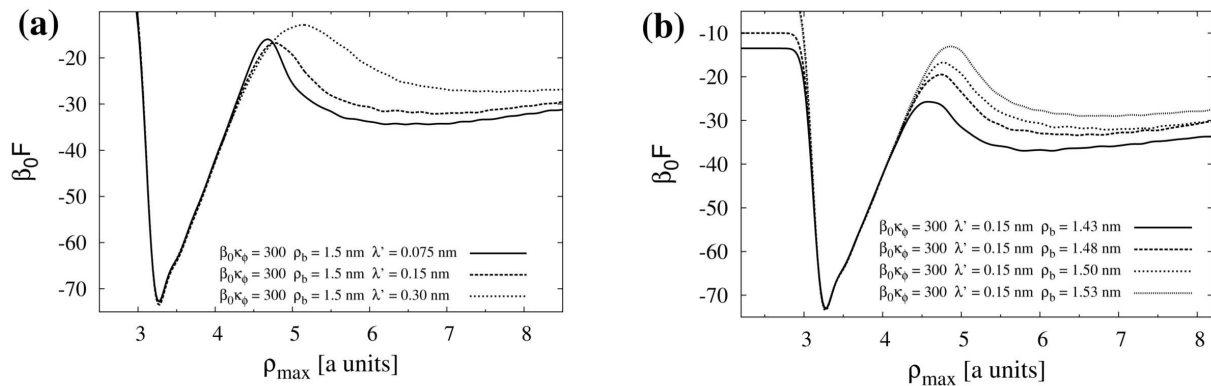


FIG. 9. Evolution of the free-energy profile associated with the temperature-activated closure mechanism for $\beta_0\kappa_\phi = 300$ reconstructed with Well-Tempered MetaDynamics, and for different values of the parameters λ' and ρ_b (cf. Eq. (A3)). We see that a slight change in these values does not change qualitatively the physics of the model. In the left panel (a), the closure free-energy barrier $\beta_0\Delta F_{cl} = 18.6, 15.4,$ and 14.3 for $\lambda' = 0.075$ nm, 0.15 nm, and 0.30 nm. In the right panel (b), $\beta_0\Delta F_{cl} = 11.2, 13.9, 14.7$ and 15.6 for $\rho_b = 1.43$ nm, 1.48 nm, 1.50 nm and 1.53 nm, respectively.

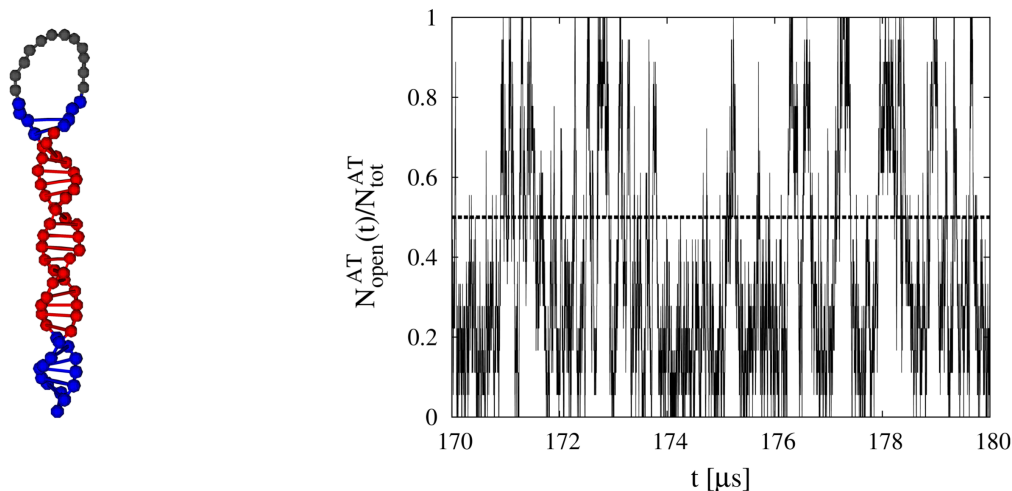


FIG. 10. Left panel: Snapshot of an equilibrated DNA beacon of sequence $5' - GCGCG(AT)_9GCGC(T)_{12}CGCG(AT)_9CGCGC - 3'$, analogous to the sequence considered in Ref. 11, in a closed configuration. The GC-rich regions are colored in blue, the middle AT-base-pair region in red, and the loop T-rich region in gray. Right panel: illustration of the temporal evolution of the number of opened AT-bps, $N_{open}^{AT}(t)/N_{tot}^{AT}$, at $T = T_m^{AT}$, associated with the internal-tagging. The dashed line represents half of the number of AT-bps in the middle domain, $N_{open}^{AT}(t)/N_{tot}^{AT} = 1/2$. We consider the middle AT-domain and the terminal GC-domain to measure the melting temperatures T_m^{AT} and T_m^{GC} , respectively.

necessary that the CVs chosen in metaD properly account for all the states and barriers. Actually, they must mainly account for the *relevant* barriers associated with coarse-grained variables on which the free-energy dependence is the most important. In the particular case of the slow closure mechanism of bubble denaturation studied in this Letter with the mesoscopic model, several observables come out to describe the metastable state as well as the transition to the closed state: (1) the length $L(t)$ of the bubble, *i.e.* the number of opened base-pairs, (2) the width $\rho_{max}(t)$ of the bubble, *i.e.* the maximal distance between paired bases, (3) the average twist angle

per bp, $\Delta\phi$, in the bubble¹⁰, and (4) the minimal twist angle, $\phi_{min}(t)$, in the bubble. As shown in Fig. 11 and Fig. 12, the observables $\rho_{max}(t)$ and $\phi_{min}(t)$ are highly correlated to the length of the bubble, $L(t)$. This property is due to the relative simplicity of the mesoscopic model for which the stacking interaction is internally described. Thus, a natural candidate for a relevant CV could be either the length $L(t)$ of the bubble itself, either its width $\rho_{max}(t)$. In the following we choose for numerical efficiency the width $\rho_{max}(t)$ as CV to bias the dynamics of the system. According to the algorithm introduced by Barducci *et al.*^{28,42} a Gaussian is deposited

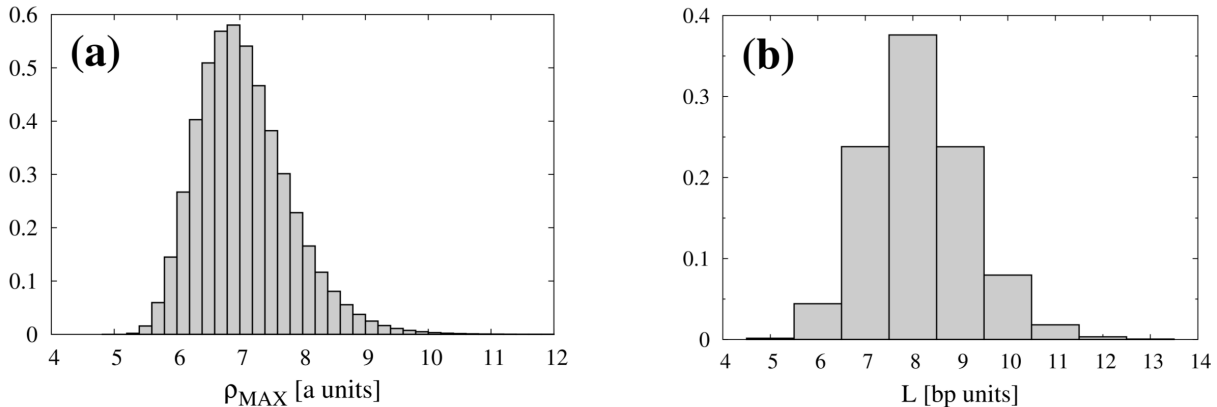


FIG. 11. Distribution of the width ρ_{\max} (a) and the length L (b) of the metastable bubble, respectively, for $\beta_0\kappa_\phi = 300$ and $\rho_b = 1.50$ nm, performed over a $60\ \mu\text{s}$ unbiased trajectory at room temperature.

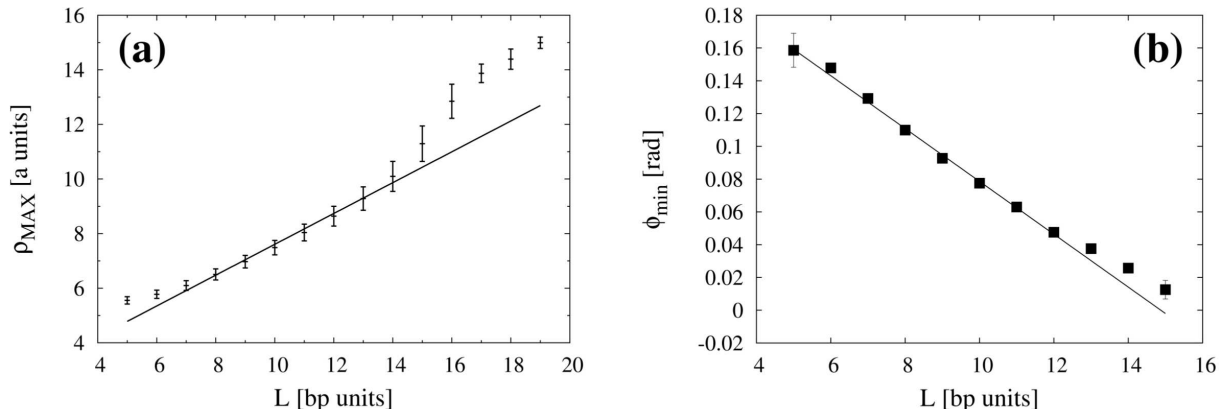


FIG. 12. Average width ρ_{\max} (a) and average minimal twist angle ϕ_{\min} (b) of the metastable bubble as a function of the number of opened base-pairs L , for $\beta_0\kappa_\phi = 300$ and $\rho_b = 1.50$ nm, and performed over a $60\ \mu\text{s}$ unbiased trajectory at room temperature (with standard deviation). We emphasize the linear interpolation in the range of L (respectively ρ_{\max} and ϕ_{\min}) defining the metastable bubble.

every $\tau_G = 25$ ps with height $w = w_0 e^{-V(s,t)/(f-1)T}$, where s is the CV, $w_0 = 0.1 k_B T$ is the initial height, T is the temperature of the simulation, $V(s, t)$ the metadynamics time-dependent bias

$$V(s, t) = \omega \sum_{t' < t} \exp \left[-\frac{(s(t) - s(t'))^2}{2\sigma^2} \right] \quad (\text{C1})$$

and $f \equiv (T + \Delta T)/T = 5$ is the bias factor with ΔT a parameter with the dimension of a temperature. The resolution of the recovered free-energy landscape is determined by the width of the Gaussians $\sigma = 0.1$ in units of the respective CV. Considering preliminary results of unbiased simulations (see Fig. 11), we put a wall at $\rho_{\max} \approx 10$ to prevent the system to escape from the metastable state⁵³ (and therefore entering in the zipping regime, *i.e.* a far from equilibrium process^{10,41}). We have checked that a slight change in the position of the wall ($\rho_{\max} = 9, 10, 11, 16, 20$) does not change significantly the results, particularly the positions of the

local minimum and the saddle, as well as the barrier height. The simulations are run until the free-energy profile does not change more than $2 k_B T$ in the last 100 ns. To further control the error of the reconstructed landscape we performed 5 runs of WT-metaD for each values of the parameter κ_ϕ . The other observables are reconstructed afterwards using the *reweighting technique* of Bonomi et al.⁴². Biased simulations were performed using the version 1.3 of the plugin for free-energy calculation, named PLUMED⁵³.

Dynamical properties. In order to estimate the mean transition times between the metastable (bubble) and the equilibrium (closed) states, we extend the *standard* application scope of metaD considering the recent method of Parrinello, Salvalaglio and Tiwary^{34,35}. We denote by τ the mean transition time over the barrier from the metastable state to the closed state, and by τ_M the mean transition time for the metadynamics run. The later changes as the simulation progresses

and is linked to the former through the acceleration factor $\alpha(t) \equiv \langle e^{\beta V(s,t)} \rangle_M = \tau/\tau_M(t)$, where the angular brackets $\langle \dots \rangle_M$ denote an average over a metadynamics run confined to the metastable basin, and $V(s,t)$ is the metadynamics time-dependent bias. To satisfy the main validity criterions, *ie.* 1) to consider a set of CVs able to distinguish between the different metastable states³⁵, and 2) to avoid depositing bias in the Transition State region³⁴, we check that the statistics of transition times follows a Poisson distribution (performing a two-sample Kolmogorov-Smirnov test with p -values in a range [0.59,0.96]), and increase the time lag between two successive Gaussian depositions $\tau_G = 600$ ps. We performed several WT-metaD simulations and stop the simulations when the crossing of the barrier and the Gaussian deposition occur unlikely at the same time. We have checked that the position of the wall does not affect the mean escape time, when put at a distance greater than the one defining the upper value of the metastable state, *ie.* $\rho_{\text{wall}} > 10$ (see Fig. 11). Actually, increasing significantly the time lag between 2 successive Gaussian depositions, one checks that the system is weakly perturbed at the border of the metastable basin only. This analysis thus highlights the value of $\beta\kappa_\phi = 540$ associated with characteristic time scales, $\tau_{\text{cl}} \approx 40 \mu\text{s}$ and $\tau_{\text{nuc}} \approx 15$ ms, for the closure and nucleation mechanisms, in good agreement with experiments¹¹.

Measure of the effective torsional modulus, $\kappa_\phi^*(L)$. Considering the equipartition theorem, we measure $\kappa_\phi^* = k_B T / \langle (\Phi - \langle \Phi \rangle)^2 \rangle$, where $\Phi \equiv \sum_{i \in \text{bubble}} \phi_i$ is the twist angle measured *consecutively* between the bps defining each extremity of the bubble and L is the length of the bubble. We clearly see in Fig. 13 that κ_ϕ^* increases when L decreases, recovering the value of the torsional modulus in the double-stranded domain, $\kappa_{\phi,\text{ds}}^* \simeq 470 k_B T_0$ (for $\beta_0 \kappa_\phi = 580$). Figure 13 highlights a non-trivial power law behaviour, $\kappa_\phi^*(L) \propto L^{-\alpha}$ with $\alpha = 2.2 \pm 0.1$. This law is valid down to $L \approx 3$ bps that corresponds to the breathing bubble regime. The origin of the free-energy barrier is indeed related to the finite value of $\kappa_\phi^*(L)$ in the metastable bubble and the crossover between two minima for the minimal twist angle, $\phi_{\text{min}}^{\text{eq}}$ and 0.

Computation of the minimal free-energy path.

To obtain a typical minimal free-energy path (as in Fig. 1 in the main text), we applied the following methodology. We considered the free-energy surface reconstructed with Well-Tempered Metadynamics. We then fixed an *initial point* located around the saddle region, *ie.* $\rho_{\text{max}} = 1.35$ nm and $\phi_{\text{min}} = 0.35$. Finally, we explored the trajectories associated with this initial point, and that drive the system to the metastable and equilibrium basins. Due to the inherent discretization scheme, this path is defined with relative accuracy (bin-size effect).

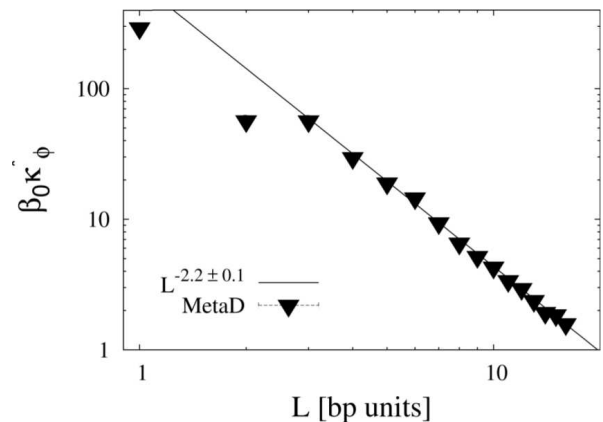


FIG. 13. Bubble torsional modulus $\kappa_\phi^*(L)$ of the metastable bubble computed using a standard metadynamics simulation with a wall at $\rho_{\text{max}} \approx 20$.

- ¹A. Kornberg and T.A. Baker, *DNA Replication* (W.H. Freeman, New York, 1992).
- ²R. Phillips, J. Kondev, J. Theriot, *Physical Biology of the Cell* (Garland Science, 2009).
- ³J.F. Léger, J. Robert, L. Bourdieu, D. Chatenay, and J.F. Marko, Proc. Natl. Acad. Sci. U.S.A. **95**, 12295 (1998).
- ⁴D. Kowalski, D.A. Natale, and M.J. Eddy, Proc. Natl. Acad. Sci. U.S.A. **85**, 9464 (1988).
- ⁵J. SantaLucia, Proc. Natl. Acad. Sci. U.S.A. **95**, 1460 (1998).
- ⁶D. Poland and H.R. Scheraga, *Theory of Helix Coil Transition in Biopolymers* (Academic Press, New York, 1970).
- ⁷C.J. Benham, Proc. Natl. Acad. Sci. U.S.A. **76**, 3870 (1979).
- ⁸J.-H. Jeon, J. Adamcik, G. Dietler, and R. Metzler, Phys. Rev. Lett. **105**, 208101 (2010).
- ⁹M. Manghi, J. Palmeri, and N. Destainville, J. Phys.: Condens. Matter **21**, 034104 (2009).
- ¹⁰A.K. Dasanna, N. Destainville, J. Palmeri, and M. Manghi, Phys. Rev. E **87**, 052703 (2013).
- ¹¹G. Altan-Bonnet, A. Libchaber, and O. Krichevsky, Phys. Rev. Lett. **90**, 138101 (2003).
- ¹²T.E. Cheatham and P.A. Kollman, J. Mol. Biol. **259**, 434 (1996).
- ¹³S.B. Dixit, D.L. Beveridge, D.A. Case, T.E. Cheatham, E. Giudice, F. Lankas, R. Lavery, J.H. Maddocks, R. Osman, H. Sklenar, K.M. Thayer, and P. Varnai, Biophys. J. **89**, 3721 (2005).
- ¹⁴S. Kannan and M. Zacharias, Phys. Chem. Chem. Phys. **11**, 10589 (2009).
- ¹⁵M. Sayar, B. Avşaroğlu, and A. Kabakçioğlu, Phys. Rev. E **81**, 041916 (2010).
- ¹⁶T.E. Ouldridge, A.A. Louis, and J.P. Doye, J. Chem. Phys. **134**, 085101 (2011).
- ¹⁷A. Savelyev and G.A. Papoian, Proc. Natl. Acad. Sci. U.S.A. **107**, 20340 (2010).
- ¹⁸S.W. Englander, N.R. Kallenbach, A.J. Heeger, J.A. Krumhansl, and S. Litwin, Proc. Natl. Acad. Sci. U.S.A. **77**, 7222 (1980).
- ¹⁹A. Zeida, M.R. Machado, P.D. Dans, and S. Pantano, Phys. Rev. E **86**, 021903 (2012).
- ²⁰M. Peyrard and A.R. Bishop, Phys. Rev. Lett. **62**, 2755 (1989).
- ²¹M. Barbi, S. Cocco, and M. Peyrard, Phys. Lett. A **253**, 5178 (1999).
- ²²J.-H. Jeon, W. Sung, and F.H. Ree, J. Chem. Phys. **124**, 164905 (2006).
- ²³A. Bar, Y. Kafri, and D. Mukamel, Phys. Rev. Lett. **98**, 038103 (2007).
- ²⁴H.C. Fogedby and R. Metzler, Phys. Rev. Lett. **98**, 070601 (2007).
- ²⁵S. P. Mielke, N. Gronbeck-Jensen, V. V. Krishnan, W. H. Fink, and C. J. Benham, J. Chem. Phys. **123**, 124911 (2005).

- ²⁶A. Laio and M. Parrinello, Proc. Natl. Acad. Sci. U.S.A. **99**, 12562 (2002).
- ²⁷A. Laio and F.L. Gervasio, Rep. Prog. Phys. **71**, 126601 (2008).
- ²⁸A. Barducci, G. Bussi, and M. Parrinello, Phys. Rev. Lett. **100**, 020603 (2008).
- ²⁹J. F. Dama, M. Parrinello, and G. A. Voth, Phys. Rev. Lett. **112**, 240602 (2014).
- ³⁰A.K. Dasanna, Ph.D. thesis, Toulouse University (2013).
- ³¹S. Wärmländer, A. Sen, and M. Leijon, Biochemistry **39**, 607 (1999).
- ³²W. R. Bauer and C. J. Benham, J. Mol. Biol. **234**, 1184 (1993).
- ³³I. De Vlaminck, M. T. J. van Loenhout, L. Zweifel, J. den Blanken, K. Hooning, S. Hage, J. Kerssemakers, and C. Dekker, Molecular Cell **46**, 616 (2012).
- ³⁴P. Tiwary and M. Parrinello, Phys. Rev. Lett. **111**, 230602 (2013).
- ³⁵M. Salvalaglio, P. Tiwary, and M. Parrinello, J. Chem. Theory Comput. **10**, 1420 (2014).
- ³⁶Z. Qi, R.A. Pugh, M. Spies, and Y.R. Chemla, eLife **2**, e00334 (2013).
- ³⁷S. Myong, M.M. Bruno, A.M. Pyle, and T. Ha, Science **317**, 513 (2007).
- ³⁸A.Y. Grosberg and A.R. Khokhlov, *Statistical Physics of Macromolecules* (AIP, Melville, NY, 1994).
- ³⁹The length of the AT-rich region only plays a role during the zipping process, and does not influence the height of the activation barriers, as long as it is greater than the typical size of the metastable bubble (see Ref. 10). Considering smaller AT tracts shifts the departure from the metastable basin to lower ρ_{\max} , consequently decreasing the height of the closure free-energy barrier.
- ⁴⁰Z. Bryant, M.D. Stone, J. Gore, S.B. Smith, N.R. Cozzarelli, and C. Bustamante, Nature **142**, 338 (2003).
- ⁴¹A.K. Dasanna, N. Destainville, J. Palmeri, and M. Manghi, EPL **98**, 38002 (2012).
- ⁴²M. Bonomi, A. Barducci, and M. Parrinello, J. Comput. Chem. **30**, 1615 (2009).
- ⁴³P. Hänggi, P. Talkner, and M. Borkovec, Rev. Mod. Phys. **62**, 251 (1990).
- ⁴⁴G. Bonnet, O. Krichevsky, and A. Libchaber, Proc. Natl. Acad. Sci. U.S.A. **95**, 8602 (1998).
- ⁴⁵J. Sponer, J. Leszczynski, and P. Hobza, Biopolymers **61**, 2 (2002).
- ⁴⁶M. Manghi, Y-W. Kim, X. Schlagberger, and R.R. Netz, Soft Matter **2**, 653 (2006).
- ⁴⁷L. F. Liu and J. C. Wang, Proc. Natl. Acad. Sci. U.S.A. **84**, 7024 (1987).
- ⁴⁸G.A. Michelotti, E.F. Michelotti, A. Pullner, R.C. Duncan, D. Eick, and D. Levens, Mol. Cell. Biol. **16**, 2656 (1996).
- ⁴⁹F. Kouzine, D. Wojtowicz, A. Yamane, W. Resch, K.-R. Kieffer-Kwon, R. Bandle, S. Nelson, H. Nakahashi, P. Awasthi, L. Feigenbaum, H. Menoni, J. Hoeijmakers, W. Vermeulen, H. Ge, T. M. Przytycka, D. Levens, and R. Casellas, Cell **153**, 988 (2013).
- ⁵⁰D. Bikard, C. Loot, Z. Baharoglu, and D. Mazel, Microbiol. Mol. Biol. Rev. **74**, 570 (2010).
- ⁵¹B.S. Alexandrov, V. Gelev, S.W. Yoo, A.R. Bishop, K. Rasmussen, and A. Usheva, PLoS Comput. Biol. **5**, e1000313 (2009).
- ⁵²J.-H. Jeon, W. Sung, Biophys. J. **95**, 3600 (2008).
- ⁵³M. Bonomi, D. Branduardi, G. Bussi, C. Camilloni, D. Provasi, P. Raiteri, D. Donadjo, F. Marinelli, F. Pietrucci, R.A. Broglia, and M. Parrinello, Comput. Phys. Comm. **180**, 1961 (2009).
- ⁵⁴T. Hugel, M. Rief, M. Seitz, H.E. Gaub, and R. Netz, Phys. Rev. Lett. **94**, 048301 (2005).
- ⁵⁵B. Tinland, A. Pluen, J. Sturm, and G. Weill, Macromol. **30**, 5763 (1997).
- ⁵⁶T. Murtola, A. Bunker, I. Vattulainen, M. Deserno, and M. Karttunen, Phys. Chem. Chem. Phys. **11**, 1869 (2009).
- ⁵⁷C. Bustamante, S.B. Smith, J. Liphardt, and D. Smith, Curr. Opin. Struct. Biol. **10**, 279 (2000).